Shock loading of carbon nanotube bundle

L. Kh. Galiakhmetova[1,2], D. V. Bachurin[1,3], E. A. Korznikova[2,4], A. M. Bayazitov[2,5], A. A. Kudreyko[6], and S. V. Dmitriev[2,5*]

[1] *Institute for Metals Superplasticity Problems, RAS, 450001 Ufa, Russia*
[2] *Institute of Molecule and Crystal Physics, UFRC, RAS, 450075 Ufa, Russia*
[3] *Institute for Applied Materials – Applied Materials Physics, Karlsruhe Institute of Technology, 76344 Eggenstein-Leopoldshafen, Germany*
[4] *Ufa State Aviation Technical University, 450008 Ufa, Russia*
[5] *Federal Research Center Institute of Applied Physics of RAS, 603950 Nizhny Novgorod, Russia and*
[6] *Department of Medical Physics and Informatics, Bashkir State Medical University, 450008 Ufa, Russia*

(Dated: April 11, 2023)

A single-walled carbon nanotube (CNT) bundle under shock loading in lateral direction is studied by means of the chain model with reduced number of degrees of freedom. One or two compressive shock waves are initiated by a piston moving at a constant speed V_0. At lower piston speeds, only the faster wave front resulting in an elliptization of CNTs propagates, while at higher speeds this is followed by the slower wave front resulting in CNT collapse. Time evolution of the CNT bundle structure during compression is investigated in detail. Energy absorption rate W as a function of the piston speed V_0 is evaluated for bundles having CNTs of different diameter D. Bundles with smaller CNT diameter demonstrate a higher energy absorption rate scaling as $W \sim D^{-3}$. The rate of energy absorption increases bilinearly with V_0, and in the regime of CNT collapse the slope of the line is twice as high as in the case when only elliptization takes place. The obtained results can be useful for the development of new types of elastic dampers.

Keywords: Carbon nanotube bundle, plane strain conditions, shock compression, deformation mechanisms, protection against shock and vibration

I. INTRODUCTION

Carbon nanotubes (CNTs) have excellent mechanical properties such as high Young's modulus [1], very high strength, and ability to absorb energy [2]. CNTs are transparent [3] and good conductors of electricity [3–5] and heat [6, 7]. The unique combination of properties makes CNTs very promising for the production of polymer composites with enhanced electrical and mechanical properties [8, 9], supercapacitors [10, 11], flexible and stretchable electronic devises [3, 12], composite materials [13] and many others [14, 15].

Arrays of horizontally aligned CNTs can be produced from as grown vertically aligned CNT bundles by shear pressing, drawing and rolling methods [16–19]. At the same time, it is almost impossible to obtain perfectly aligned CNT bundles, and therefore CNT networks consisting of entangled dendritic bundles are modeled and experimentally studied [20–22]. Single-walled CNT bundles are linear elastic up to 1.5 GPa hydrostatic pressure at room temperature and demonstrate the volume compressibility of 0.024 GPa^{-1} [23]. It has been shown that the deformation of CNT bundles under non-hydrostatic loading becomes irreversible for pressures above 5 GPa [24]. The results of experimental and numerical studies on mechanical properties of CNTs have been summarized in the work [25]. Lateral quasi-static compression of CNTs and graphene has been analyzed, e.g., in Refs. [26–31].

The mechanical properties of graphene sheets and CNTs have been investigated under quasi-static conditions, but their behavior under extreme dynamic loading has been studied much less. Below is a brief overview of some experimental and theoretical works devoted to the dynamical response of carbon nanomaterials.

From miniaturized ballistic tests at 600 m/s it is known that the specific penetration energy for multilayer graphene is about 10 times higher than that for macroscopic steel sheets [32]. Mechanical behavior of graphene under the impact of silica and the nickel nanoprojectiles moving with the velocity of 5 km/s was modelled, and a large amount of energy absorbed during the deformation was attributed to the superior ultimate stress and strain of graphene [33].

Molecular dynamics simulations of the impact of one, two and three layers of graphene with a fullerene rigid projectile was performed for the impact velocity in the range of 3.5 to 7.5 km/s [34]. Initiation of two to three in-plane cracks in the graphene sheet was detected. The impact dynamics of a fullerene molecule and a single-layered graphene sheet was examined with the use of an analytical approach based on nonlocal theory of thin plates and molecular dynamics [35]. The ability of a suspended graphene sheet to capture a projectile in

* Correspondence email address: dmitriev.sergey.v@gmail.com

the form of a single-walled carbon nanotube was analyzed by Yang and Tong in Ref. [36]. In particular, it was demonstrated that the projectile induces longitudinal and transverse wave fronts in graphene. As a result of such impact, graphene absorbs 89-100% of the projectile's kinetic energy. The latter means that graphene can effectively trap high-speed nanoparticles or molecules. In-plane shock waves in graphene and boron nitride were analyzed by Shepelev *et al.* [37]. The authors showed that the shock waves propagate longer distances in boron nitride as compared to graphene and associated with the scattering of the excitation energy by lattice phonons.

In works devoted to the dynamical loading of two-dimensional materials, a significant effect of the strain rate has been revealed. For example, in the experimental work [38], it was shown that CNTs under compression by a shock wave are damaged much more heavily than under static compression. Graphene can absorb the energy of shock waves without failure [39] or it can act as an interlayer reflecting shock waves [40]. Structure evolution of nanoscrolls, fullerenes and nanotubes during a collision with an obstacle was analyzed in Refs. [35, 36, 41]. A study of the Ni projectile penetration into a few-layered graphene for an impact velocity of 900 m/s was performed in Ref. [42] with subsequent comparison with experimental data. The addition of CNTs to the Kevlar fabric results in an increase of the resistance of epoxy composites to penetration of steel projectiles [43].

Composite materials reinforced with CNTs are very effective in absorbing the energy of shock waves and vibrations [44–48], as well as protecting against thermal shocks [49–51].

Efficient modeling of CNT-based structures requires the development of new computational approaches in addition to the classical molecular dynamics method. Mesoscopic modeling has been applied to the study of deformation mechanisms of CNT forest [52, 53]. Large deformations of CNTs can be described using a continuum beam and thin shell theories [54–56]. The mechanical properties of CNTs under transverse loads were studied in Ref. [57]. The mechanical properties and failure of the CNT bundles were modelled using the nonlinear coarse-grained stretching and bending potentials [58].

It is known that CNTs, the diameter of which exceeds the threshold value D_c, can have either a circular or collapsed cross section, and the stability of the latter is ensured by the van der Waals forces [59–62]. It was shown that the critical diameter of an individual CNT differs from the critical diameter of CNTs in a bundle [63]. In particular, for the single-, double-, and triple-walled CNTs, the authors report values of 34, 48, and 60 Å. In the paper [64] energetically preferable packings of collapsed CNTs were found.

In contrast to dense materials, CNT bundles can demonstrate very high compressibility in the elastic region and therefore can be used as a protection material against shocks and vibrations [65–67]. In this work, we analyze a single-walled CNT bundle subjected to high-speed lateral compression in order to reveal its ability to absorb an impact energy. The chain model with reduced number of degrees of freedom proposed by Savin and co-authors [68] and modified for the CNT bundle in Ref. [69] is employed. The efficiency of the chain model in modelling secondary sp^2-carbon structures has been verified in a number of publications [68–77]. Our model neglects several very important structural peculiarities of real CNT bundles such as CNT entanglement, dispersion of their diameters and existence of multi-walled CNTs. The aim of our study was to show the possibility of energy absorption by the CNT bundles and for the first study we have chosen the simplest possible model.

In Sec. II we describe the computational model and in Sec. III the simulation setup. Simulation results are presented in Sec. IV and conclusions are drown in Sec. V.

II. MODEL

Dynamic uniaxial compression of the zigzag CNT bundle is considered under plane strain condition. Cross-sections of CNTs create a triangular lattice in the xy plane (see Fig. 1). Each carbon atom belonging to the cross section of a CNT is a member of a rigid chain of atoms perpendicular to the xy plane. ρ is the equilibrium interatomic distance in the zigzag CNT wall. $a = \rho\sqrt{3}/2$ is the distance between neighboring atoms in projection onto the xy plane. The number of atoms in the cross section of a CNT is equal to an even number N. Small and large circles in Fig. 1 denote the two sets of the atomic chains shifted one with respect to another along the z-axis by a distance of $\rho/2$. CNT diameter is $D = a/\sin(\pi/N)$. d is the equilibrium distance between the walls of neighboring CNTs. Then $A = D + d$ is the distance between the centers of neighboring CNTs. In the considered geometry, the carbon atoms have two degrees of freedom and can move on the xy plane only.

Atoms in the computational cell are numbered by three indices: $i = 1, ..., I$ and $j = 1, ..., J$ are the indices of a CNT in a bundle, they number CNT rows and columns; the index $n = 1, ..., N$ numbers atoms within a CNT. Total number of atoms in the cell is $L = I \times J \times N$.

The Hamiltonian (total energy) of the CNT bundle includes four terms [68, 69] and can be written as

$$H = K + U_{\mathrm{B}} + U_{\mathrm{A}} + U_{\mathrm{VdW}}, \qquad (1)$$

where K is the kinetic energy and the other three terms in the right-hand side give the potential energy, which

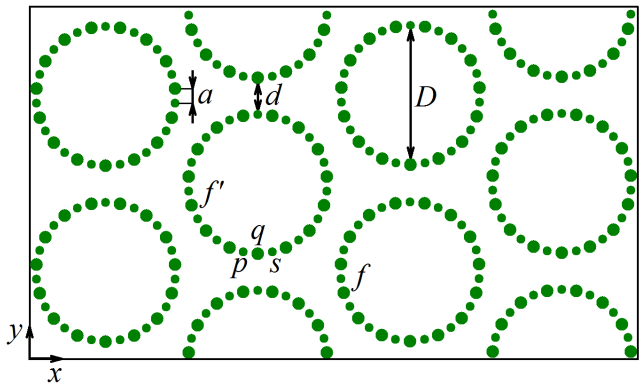

Figure 1. Computational cell with $I \times J$ CNTs ($I = 4$ and $J = 2$ in this case, while $I = 200$, $J = 8$ is used in the simulations). Each zigzag CNT is represented by N carbon atoms that move along the xy plane. The case of $N = 30$ is shown. Each atom stands for a rigid row of atoms perpendicular to the xy plane. Small and large circles show the two types of the rigid rows shifted one with respect to another along the z-axis. Here a denotes the distance between carbon atoms in the wall of a CNT, neighboring CNTs are separated by a distance d, D is CNT diameter and $A = D + d$ is the distance between centers of neighboring CNTs. Indices p, q, s, f, and f' are used to describe the interactions between atoms (see description in the text).

consists of the energy of valence bonds U_B, the energy of valence angles U_A, and the energy of van der Waals interactions $U_{\rm VdW}$. All these four terms are described in Ref. [69] and we describe them here for the convenience of the reader. In Fig. 1, indices p, q, and s number nearest atoms of a CNT, f is the atom belonging to a different CNT. Atoms q and f' belong to the same CNT, but the distance between them is not less than $3a$. Then the energies in the right-hand side of Eq. (1) are calculated as follows.

Kinetic energy is

$$K = \frac{M}{2}\sum_{l=1}^{L}|\dot{\mathbf{r}}_l|^2, \qquad (2)$$

where M is the carbon atom mass, $\mathbf{r}_l$ is the radius-vector of l-th atom, overdot means differentiation with respect to time, and summation is performed over all atoms in the system.

The energy of valence bonds is

$$U_{\rm B} = \sum_{i=1}^{I}\sum_{j=1}^{J}\sum_{q=1}^{N}\frac{\alpha}{2}(|\mathbf{r}_{i,j,q} - \mathbf{r}_{i,j,s}| - a)^2, \qquad (3)$$

which is summation over the bonds connecting nearest atoms (see Fig. 1) and the number of such bonds is equal to the number of atoms in the computational cell. In Eq. (3), α is the valence bond stiffness.

The energy of valence angles is given by the anharmonic potential

$$U_{\rm A} = \sum_{i=1}^{I}\sum_{j=1}^{J}\sum_{q=1}^{N}\epsilon[1 + \cos\theta_{pqs}],$$
$$\cos\theta_{pqs} = \frac{(\mathbf{r}_{i,j,q} - \mathbf{r}_{i,j,p}, \mathbf{r}_{i,j,s} - \mathbf{r}_{i,j,q})}{|\mathbf{r}_{i,j,q} - \mathbf{r}_{i,j,p}||\mathbf{r}_{i,j,s} - \mathbf{r}_{i,j,q}|}, \qquad (4)$$

where summation is over the valence angles formed by the atoms p, q, and s (see Fig. 1), and the number of such angles is equal to the number of atoms in the computational cell.

The energy of van der Waals interactions is described by the (5,11) Lennard-Jones potential

$$U_{\rm VdW} = \frac{1}{2}\sum_{q,f=1;\,q\neq f}^{N}\frac{\varepsilon}{6}\Big[5\Big(\frac{\sigma}{|\mathbf{r}_q - \mathbf{r}_f|}\Big)^{11} - 11\Big(\frac{\sigma}{|\mathbf{r}_q - \mathbf{r}_f|}\Big)^{5}\Big]. \qquad (5)$$

Here summation is over all interatomic bonds connecting atoms q and f belonging to different CNTs and atoms s and f' belonging to the same CNT (see Fig. 1). The cut-off radius for the van der Waals interactions is 6 Å. As it was already mentioned, the bonds shorter than $3a$ are not taken into account for the atoms s and f' belonging to the same CNT.

The equations of motion are derived from the Hamiltonian Eq. (1) using the Hamilton's principle. The result reads

$$M\ddot{\mathbf{r}}_l = -\frac{\partial U_{\rm B}}{\partial \mathbf{r}_l} - \frac{\partial U_{\rm A}}{\partial \mathbf{r}_l} - \frac{\partial U_{\rm VdW}}{\partial \mathbf{r}_l}, \qquad (6)$$

where index $l = 1, ..., L$ numbers atoms of the computational cell, $L = IJN$.

The units of time, energy and distance in our simulations are picoseconds, electron volt, and angstrom, respectively. In these units the mass of carbon atom in Eq. (2) is $M = 12 \times 1.0364 \times 10^{-4}$ eVps^2/Å^2. The valence bond stiffness in Eq. (3) is $\alpha = 405$ N/m [68], which in the units adopted here gives $\alpha = 25.279$ eV/Å^2. Valence angle stiffness in Eq. (4) is $\epsilon = 3.50$ eV [68]. Parameters of Eq. (5) are $\varepsilon = 0.00166$ eV and $\sigma = 3.61$ Å [68].

The accuracy of the chain model described above has been evaluated in previous studies in comparison to full atomic simulations. The work [68] analyzed the scroll configurations of carbon nanoribbons and demonstrated very good agreement between the full atomic and reduced models when simulating the radial thermal expansion of scrolls. Similarly, good agreement between the two models was demonstrated in modeling the dynamics of ripplocations formed by graphene nanoribbons on a graphite substrate [70]. The accuracy of the chain model is high when the deformation of nanoribbons or CNTs is close to plane strain conditions. On

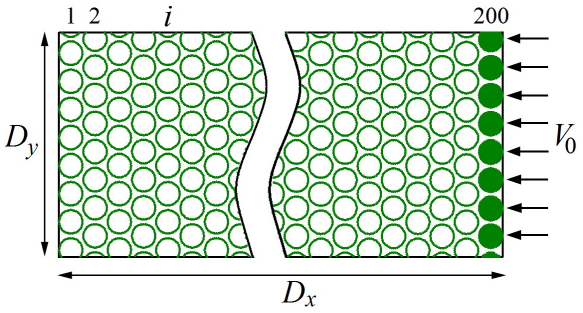

Figure 2. Computational cell with dimensions D_x and D_y used for simulation of shock loading. The cell includes 200 vertical rows of CNTs and 8 CNTs in each row. Vertical rows are numbered by the index $i = 1, ..., 200$. CNTs are parallel to the z-axis and their lateral compression is considered under plane strain conditions. CNT centers create a triangular lattice in the xy plane. Periodic boundary conditions are applied along the y-axis. Free surface is at the left side of the computational cell. The vertical row at the right end of the cell ($i = 200$) at the initial moment of time $t = 0$ starts to move to the left with the constant velocity of V_0 as the rigid body (shown by filled circles).

the other hand, the chain model is inapplicable, for example, to modeling CNT bundles with entangled CNTs, since in this case the assumption of plane strain is not satisfied.

The parameters of the chain model were chosen to reproduce acoustic longitudinal (LA) and transverse (ZA) phonon dispersion curves in the long-wavelength region [68]. The rigidity of valence bonds and bond angles corresponds to the rigidity of graphene in tension and bending, and van der Waals interactions reproduce well the interaction between graphite layers [68]. It was shown that the chain model reproduces well the frequencies of CNT bending vibrations [78, 79].

III. SIMULATION SETUP

In this study, dynamical uniaxial compressive loading of CNT bundles is analysed under plane strain conditions as schematically shown in Fig. 2. The computational cell includes 200 vertical rows of CNTs numbered by the index $i = 1, ..., 200$ and each row includes eight CNTs numbered by the index $j = 1, ..., 8$. Periodic boundary conditions are applied in y direction. This structure is initially relaxed at zero temperature under the assumption that there are free surfaces at the left and right ends of the computational cell and no external forces are applied. Thus, the equilibrium cell sizes, i.e. D_x and D_y, are found after relaxation.

In Table I, the equilibrium geometrical parameters of the computational cells are given for different numbers of atoms representing CNT cross section: $N = 30$, 35, 40 and 45. These results are obtained taking the equilibrium interatomic distance in graphene $\rho = 1.418$ Å. The equilibrium distance between rigid atomic rows oriented along the z-axis is $a = \rho\sqrt{3}/2 = 1.228$ Å.

Table I. Summary of geometrical parameters of the computational cells used in simulations. Here N is a number of atoms in CNT cross section, D is CNT diameter, A (Å) is a distance between CNT centers, D_x and D_y are the sizes of the computational cell along the x and y axes, L is total number of atoms.

N	30	35	40	45
D (Å)	11.75	13.7	15.65	17.6
A (Å)	14.83	16.78	18.74	20.7
D_x (Å)	2600	3000	3300	3600
D_y (Å)	120	140	150	170
L	48000	56000	64000	72000

The CNT diameters considered in our study are smaller than the critical value $D_c = 34$ Å indicated in the paper [63] for single-walled nanotube bundles.

At initial moment of time $t = 0$, a rigid piston (vertical row of CNTs $i = 200$) starts to move to the left with the speed V_0. This row is depicted in Fig. 2 by filled circles illustrating CNTs. The free surface conditions at the left end of the computational cell are kept, and the simulation is continued until the disturbance from the moving piston reaches the left end of the cell. The piston velocities considered in this study are in the range of 1 to 12 Å/ps (100 to 1200 m/s).

The total energy of the "piston – CNT bundle" system is conserved. In the following, only the energy of the CNT bundle is analyzed, which increases with time, since the piston does work on it. The simulation does not use a temperature thermostat. At $t = 0$ the CNT bundle has zero temperature. In the part of the CNT bundle in front of the compressive wave initiated by the moving piston temperature remains zero and it becomes nonzero behind the wave. For selected piston speeds (up to 12 Å/ps=1200 m/s), the temperature does not exceed 1000 K, which is much lower than the melting temperature of carbon structures (about 5000 K [80]). The chain model formulated for this study cannot simulate CNT melting or fracture because valence bonds are modeled by a harmonic potential Eq. (3); but this potential can be replaced by a Morse potential so that bond breaking can be simulated if desired.

IV. SIMULATION RESULTS

Simulation of the shock compressive loading of a CNT bundle shows that immediately after the piston starts

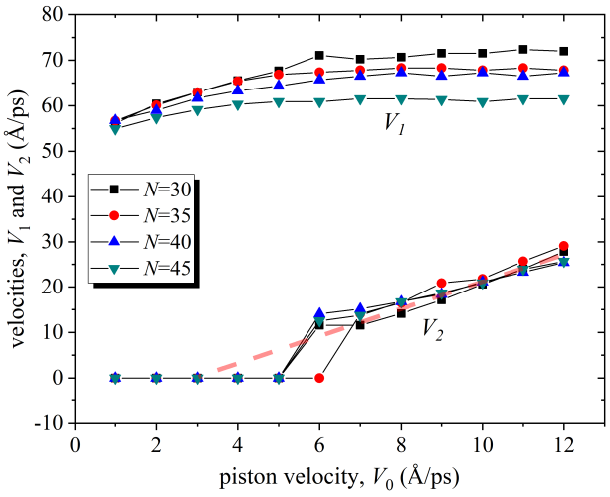

Figure 3. Dependence of the speed of the first and second compressive wave fronts, V_1 and V_2, on the piston speed V_0 for different CNT diameters (different numbers of atoms N in CNT cross section). The wave propagating with the speed V_1 changes the CNT cross sections from circular to elliptic and behind the wave propagating with speed V_2 CNTs are collapsed. The dashed line shows the linear relationship between V_2 and V_0 and is guide for the eye.

to move at $t = 0$, the compressive wave front begins to propagate with a velocity V_1; behind the front of this wave, the shape of the CNT cross section changes from circular to elliptical. If the piston speed is above the threshold value of $V_0^* = 6$ Å/ps than the second compressive wave moving with the velocity $V_2 < V_1$ is initiated, and the cross sections of CNTs behind this wave are collapsed.

Fig. 3 demonstrates how the speed of the two wave fronts (V_1 and V_2) depends on the speed of the piston V_0 for bundles containing CNTs of different diameters. Recall that CNT diameter is controlled by the number of carbon atoms N in the cross section. Two different scenarios of shock wave propagation for low and high piston speeds are clearly visible, with a threshold value of approximately $V_0^* = 6$ Å/ps, regardless of the CNT diameter.

In the scenario (1), at $V_0 < V_0^*$, the first wave front propagation speed V_1 increases linearly with increasing the piston speed V_0, and the collapse wave is not generated at all. In the scenario (2), at $V_0 > V_0^*$, velocity V_1 does not depend on V_0, but at the same time V_2 increases linearly with an increase in the piston speed. At that, the velocity V_2 does not show dependence on the CNT diameter, while V_1 decreases with increasing N. In addition, the velocity of the wave front V_1 for CNTs with a larger diameter does not change as much with an increase in the piston velocity V_0 as for CNTs of a smaller diameter. It follows from this that saturation can be expected at large CNT diameters, when the velocity V_1 practically ceases to depend on V_0.

Time evolution of the CNT bundle structure with N=40 during compressive wave propagation initiated with the piston speed of $V_0 = 3$ Å/ps, which is smaller V_0^*, is presented in Fig. 4. In order to visualize the entire computational cell, the latter is divided into five sections, which are positioned one below the other. For clarity, the wave front is indicated by the vertical blue line. In this scenario (1), i.e. when $V_0 < V_0^*$, firstly the CNTs start to compress rapidly and later they relax into various regular structures with elliptic cross-sections. In this case, no clear difference in the cross-section of the CNTs in the vicinity of the blue line is visible, i.e. a gradient structure appears.

Figure 5 illustrates the scenario (2), namely, the propagation of the compressive wave in exactly the same CNT bundle structure as in Fig. 4, but for a higher piston velocity of $V_0 = 10$ Å/ps. In this case, an excitation of the collapse wave front (shown by the vertical red lines) is observed. Three different types of structure during shock wave propagation can be distinguished in Fig. 5. (i) To the left of the blue line, the CNT cross-sections retain their circular shape, and the compressive waves do not reach this region. (ii) Between the blue and the red lines, an elliptization of CNTs takes place. (iii) To the right of the red line, collapsed CNTs are visible.

The total energy (kinetic plus potential) of carbon atoms is shown in Fig. 6 in colors from blue (zero energy level) to red (energy equal to 0.25 eV), see the color bar on the right. This result is for $N = 40$ and $V_0 = 10$ Å/ps as in Fig. 5. A part of the bundle near the boundary between the regions of CNT elliptization and collapse is presented. First, we note that the energy density in the collapsed part of the bundle is higher than in the part with elliptical CNTs. It can be concluded that collapsed CNTs absorb energy better. Second, the atoms located in the regions of CNTs with a large curvature of the cross section have the highest energy. This is due to the fact that energy is mainly stored in valence angles and not in van der Waals interactions and valence bonds [72].

Figure 7 shows the parameters that characterise the evolution of structure and energy of the CNT bundle. The results are presented for a time interval from 5 to 45 ps with a step of 5 ps. Top (bottom) panels correspond the the piston velocity V_0=3 Å/ps (V_0=10 Å/ps). All parameters are given as the functions of the vertical row number $i = 1, ..., 200$, and they are averaged over eight CNTs in each vertical row.

Fig. 7(a) shows the displacement of the centers of gravity of CNTs along the computational cell. In the top panel, propagation of the compressive waves with the speed V_1 is clearly seen. Before the wave front approaches, the centers of gravity have zero displacements.

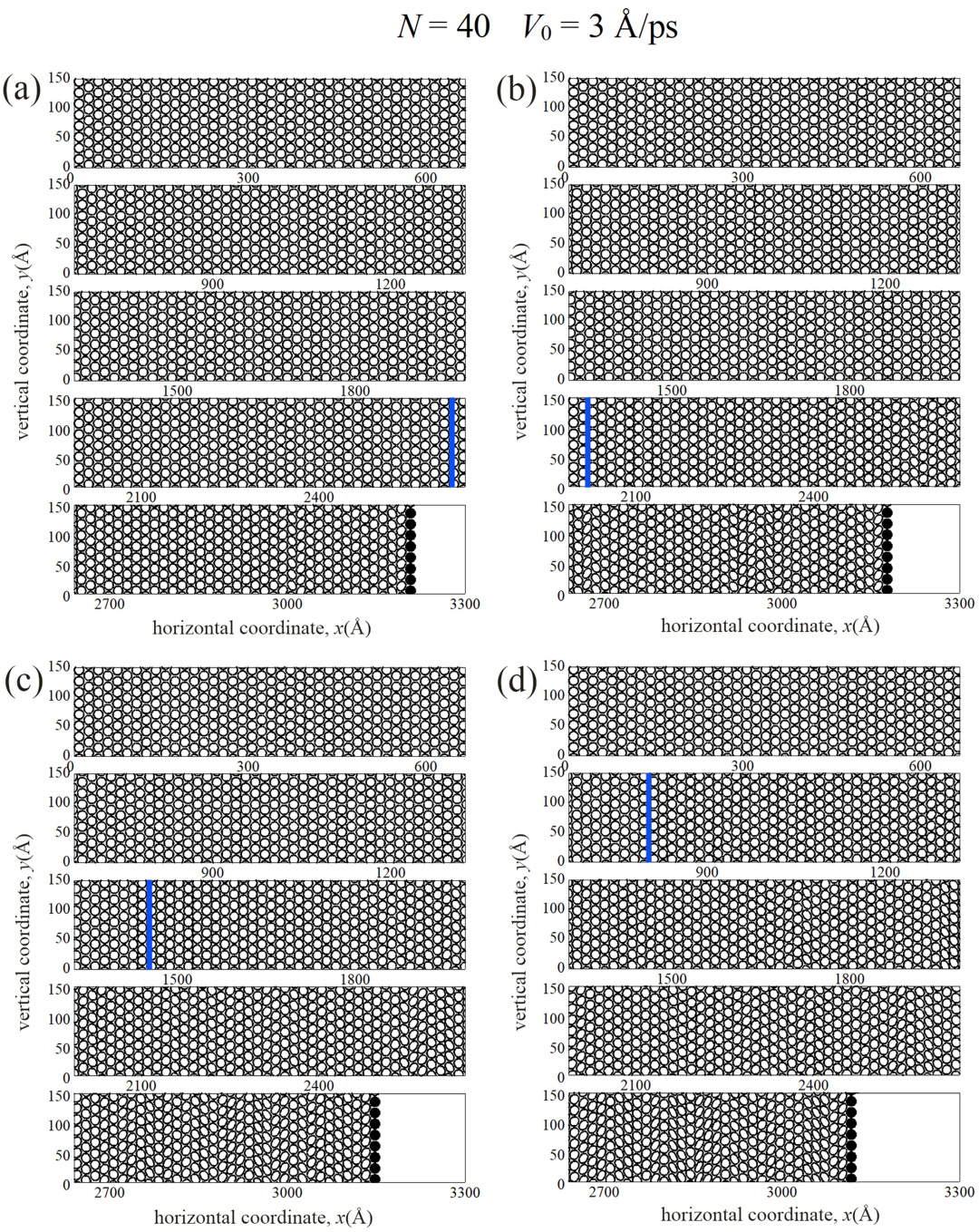

Figure 4. Evolution of the CNT bundle structure in time when compressed by a piston moving at a relatively low speed V_0=3 Å/ps: (a) t = 10 ps, (b) 20 ps, (c) 30 ps, (d) 40 ps. In this case N=40. The vertical blue lines indicate the elliptization wave front in the CNT structure. For the convenience of visual perception, the computational cell is divided into five sections, which are located one below the other. The piston is at the lower section on the right (shown by filled CNTs), and the shock wave propagates from the bottom into the top sections of the cell.

After passing the front, elliptized CNTs move with an almost constant velocity of V_1 = 61.7 Å/ps. An increase of the piston velocity up to V_0 = 10 Å/ps (see bottom panel) results in an appearance of two compressive waves. The faster wave of elliptization moves with the velocity of V_1 = 67.3 Å/ps, while the slower wave of CNT collapse with V_2 = 21.1 Å/ps. The latter fact is clearly recognized by the presence of two different slopes

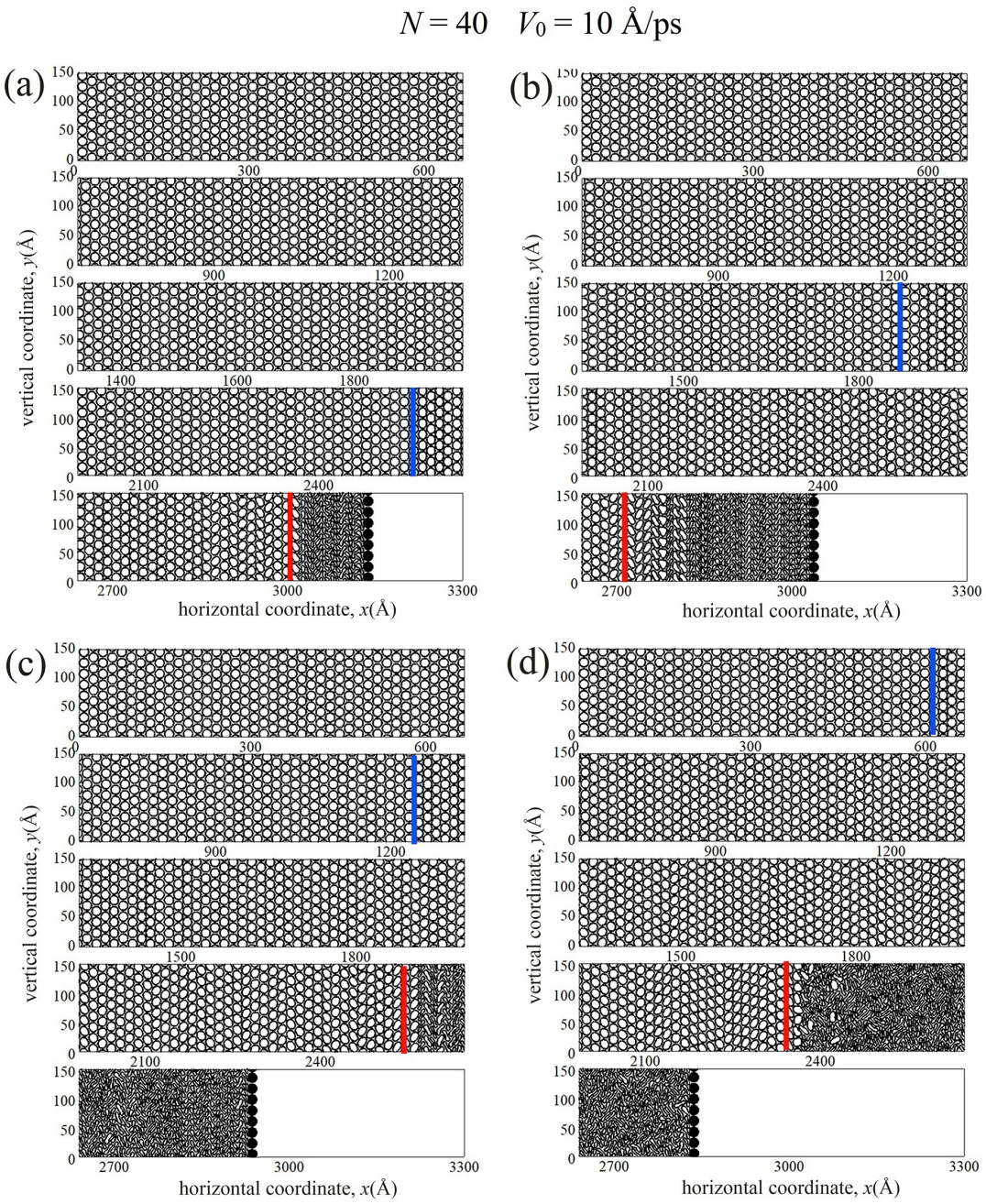

Figure 5. Evolution of the CNT bundle structure in time when compressed by a piston moving at a relatively high speed V_0=10 Å/ps: (a) t = 10 ps, (b) 20 ps, (c) 30 ps, (d) 40 ps. Here, too, N=40. The vertical blue lines indicate the faster wave front of elliptization of CNTs. The vertical red lines designate the wave front behind which CNT collapse is observed. For the convenience of visual perception, the computational cell is divided into five sections, which are located one below the other. The piston is at the lower section on the right (shown by filled CNTs), and the shock waves propagate from the bottom into the top sections of the cell.

of the displacement curves.

The characteristic of CNT ellipticity as a function of the vertical row number i for V_0=3 Å/ps is displayed in the top panel of Fig. 7(b). The ratio of the minimal to maximal diameters of CNTs $D_{\min}/D_{\max}$ is averaged over 8 CNTs for each row. Before the compression wave comes, the ratio $D_{\min}/D_{\max}$ is close to unity indicating that the CNT cross sections preserve a circular shape.

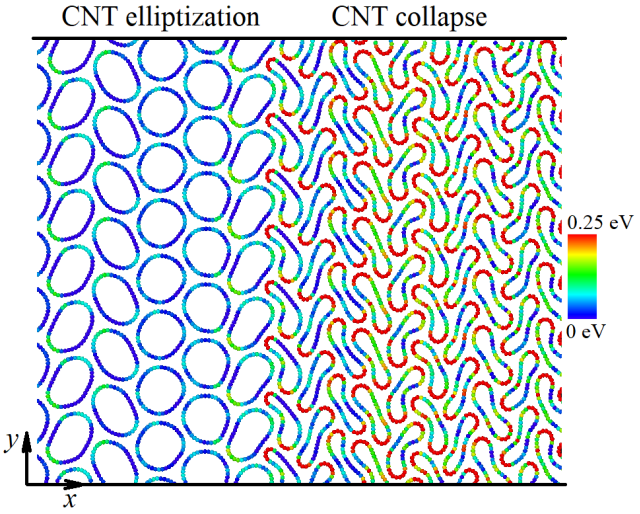

Figure 6. The total energy of the atoms color coded according to the color bar shown on the right. The left (right) part of the figure shows the bundle region behind the CNT elliptization (CNT collapse) wave. Results for $N = 40$, $V_0 = 10$ Å/ps.

Upon arrival and passage of the wave front, this ratio rapidly drops to a plateau at about of 0.95 and after some time decreases further performing oscillations. The minimal value of the ratio observed in this numerical run is circa 0.65. At higher speed of the piston, V_0=10 Å/ps (see bottom panel), after passage of the elliptization wave front, a reduction of $D_{\rm min}/D_{\rm max}$ down to about 0.8 is observed. However, when the collapse wave passes, a sharp drop of the $D_{\rm min}/D_{\rm max}$ ratio down to about 0.2 occurs. It is this value that characterizes fully collapsed CNTs in the bundle.

Potential energy per atom (averaged over eight CNTs for each row) stored by valence bonds and valence angles are presented in Figs. 7(c) and (d), respectively. As seen, before the wave comes, CNTs have nearly zero valence bond energy and valence angle energy of about 1.75 eV. The latter energy is attributed to the energy spent to bend flat graphene sheets into CNTs. Passing of the elliptization compressive wave increases $E_{\rm bond}$ up to about 0.06 eV and $E_{\rm angle}$ up to about 1.85 eV. The subsequent collapse wave (seen only in the bottom panels) increases the energy significantly, $E_{\rm bond}$ up to 0.5 eV on average and $E_{\rm angle}$ up to 5.5 eV. It should be noted that some time is needed for elliptization of CNTs in the bundle after passing the elliptization wave. Elliptization results in further increase of $E_{\rm angle}$ up to the value of 2.05 eV. The front of CNT elliptization can be seen in Fig. 7(d) as a sharp rise of $E_{\rm angle}$.

Fig. 8 demonstrates kinetic, potential, and total energies of the computational cell per particle, as the functions of time, calculated for the two different piston speeds of V_0=3 Å/ps (upper panel) and V_0=10 Å/ps (lower panel). The results are for $N = 40$. One can see that the kinetic and potential energies are nearly equal. The total energy increases slightly slower than linearly. The increase in the total energy is about 6.8 times faster for V_0=10 Å/ps as compared to the case of V_0=3 Å/ps.

From the results presented in Fig. 8 one can extract the energy absorption rate by the CNT bundle, normalized to the unit surface. It can be calculated as

$$W = \frac{LE_{tot}}{T} \times \frac{1}{3\rho D_y}, \qquad (7)$$

where the first multiplier on the right-hand side gives the total energy of the computational cell, obtained at the moment of time $t = T$, divided by the time T. The second multiplier is the inverse surface of the computational cell (parameters D_y and L are given in Table I) and ρ is the interatomic distance in the CNT wall. Genetrally, W is the energy absorption rate per unit time and unit surface of the bundle. For example, from the top panel of Fig. 8 one finds that the total energy of the computational cell per atom at $t = T = 45$ ps is E_{tot} =0.0076 eV, and the surface of the computational cell for $N = 40$ is $1/(3\rho D_y) = 1.57 \times 10^{-3}$ Å^{-2}. Then $W = 1.67 \times 10^{-2}$ eV/(ps Å^2).

The dependence of the energy absorption rate vs. the piston speed is shown in Fig. 9 for bundles with CNTs of different diameters, which is controlled by the number of carbon atoms in the CNT cross section, i.e. N. It is seen that the energy absorption rate increases with a decrease in CNT diameter. The inset shows the energy absorption rate multiplied by the cube of the CNT diameter. Since all four curves merge within the modeling error, then from this it can be concluded that $W \sim D^{-3}$.

The absorption rate also increases with increasing piston speed and can be fitted by the bilinear function, as shown by the dashed lines in the inset of Fig. 9. The lines cross at about $V_0 = 6$ Å/ps, which separates the two dynamical regimes: (1) propagation of only elliptization compressive wave and (2) propagation of the elliptization and the collapse compressive waves. The slope of the line in the second regime is 2.2 times greater than in the first one. This means that the collapse of CNTs more than doubles the rate of energy absorption.

V. CONCLUSIONS

In summary, propagation of compressive waves in a single-walled CNT bundle was investigated using the chain model with reduced number of degrees of freedom. Depending on the speed of the piston V_0, two different scenarios of shock wave propagation in the CNT bundle were revealed. At values below the threshold value of

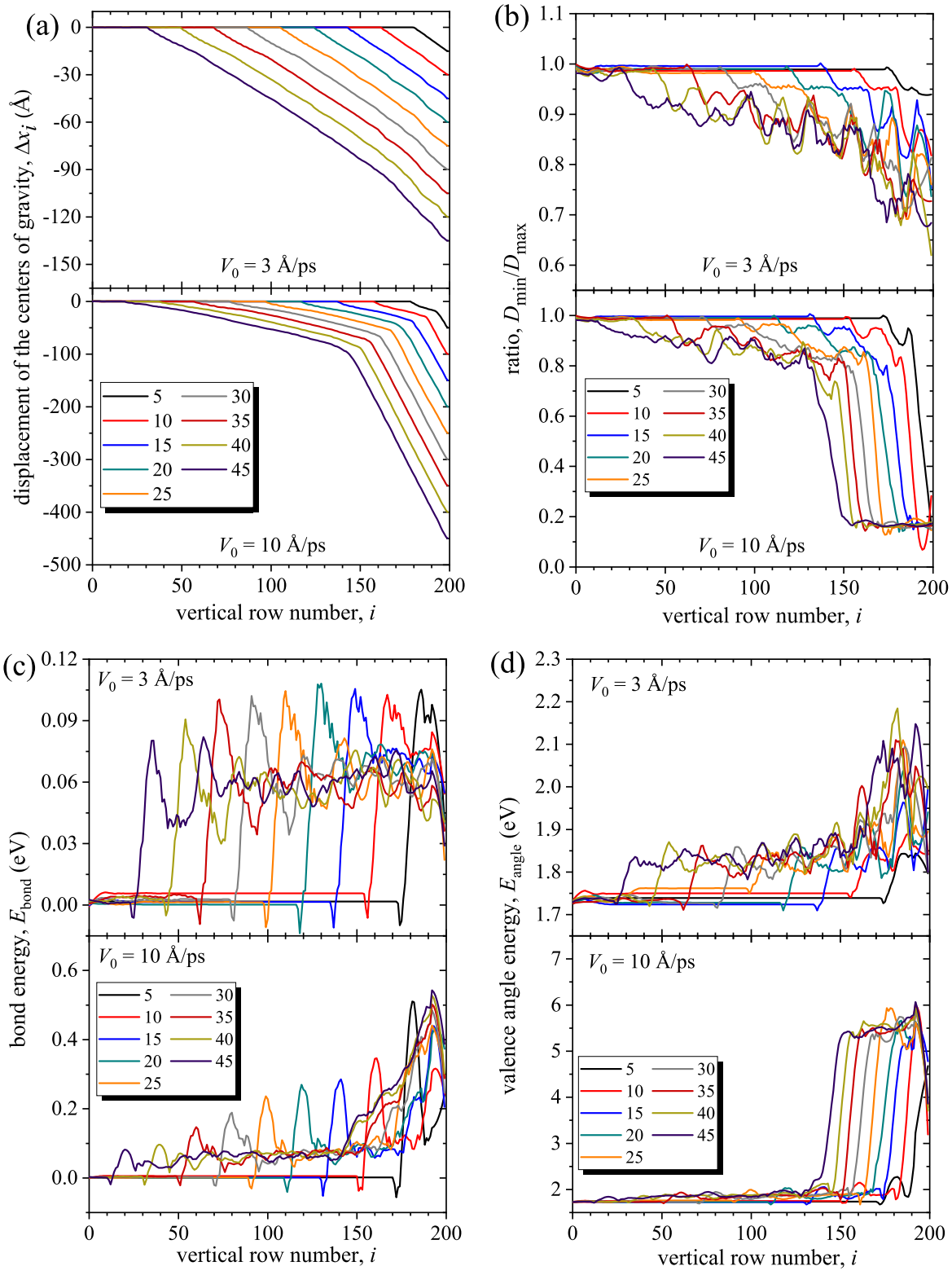

Figure 7. Distribution of structural and energy parameters along a CNT bundle during propagation of compression waves at times from 5 to 45 ps with a step of 5 ps. The parameters are averaged over eight CNTs belonging to i-th vertical row, where $i = 1, ..., 200$. (a) Displacements of the centers of gravity of CNTs along the x-axis; (b) ellipticity of CNTs, i.e. the ratio of the minimum diameter of CNTs to the maximum diameter; (c) the bond energy E_{bond} and (d) the valence angle energy E_{angle}. Upper panels of each subfigure show the results for the piston speed V_0=3 Å/ps and lower panels for V_0=10 Å/ps. For both cases N=40.

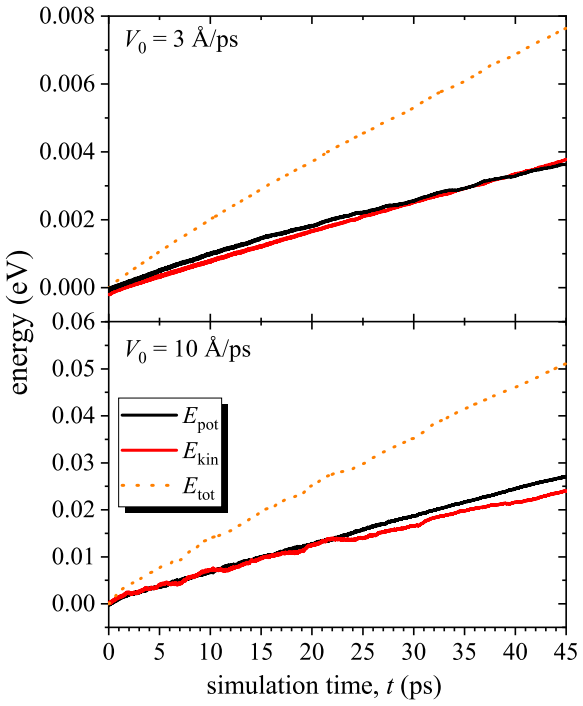

Figure 8. Increase in the potential (black solid line), kinetic (red solid line), and total (dotted orange line) energies per particle of the entire computational cell as functions of time. The top and bottom panels show the results for piston speed of V_0=3 and 10 Å/ps, respectively. For both cases N=40.

$V_0^* = 6$ Å/ps, the compressive wave propagation with the velocity V_1 followed by elliptization of CNT cross-sections was observed. This was called regime (1). In the regime (2), for $V_0 > V_0^*$, the elliptization wave was followed by a wave of CNT collapse propagating with the velocity $V_2 < V_1$.

Energy absorption rate by the CNT bundle, W, as the function of the piston speed V_0 increases with a decrease in CNT diameter as $W \sim D^{-3}$. The dependence $W(V_0)$ can be fitted by a bilinear function with two linear sections corresponding to the two modes of propagation of compressive waves. The slope in the second mode is about twice as much as in the first one. Thus, the collapse of CNTs increases the ability of CNT bundles to absorb energy of compressive wave. Note that the chain model underestimates the energy absorption of the CNT bundle because the removal of the longitudinal degrees of freedom reduces the energy absorption ability of the system.

The CNTs considered in this work have a relatively small diameter; therefore, their collapsed cross sections, after removing the load, should return to a circular shape [59–62]. This means that the CNT bundles under consideration can be repeatedly used as elastic dampers

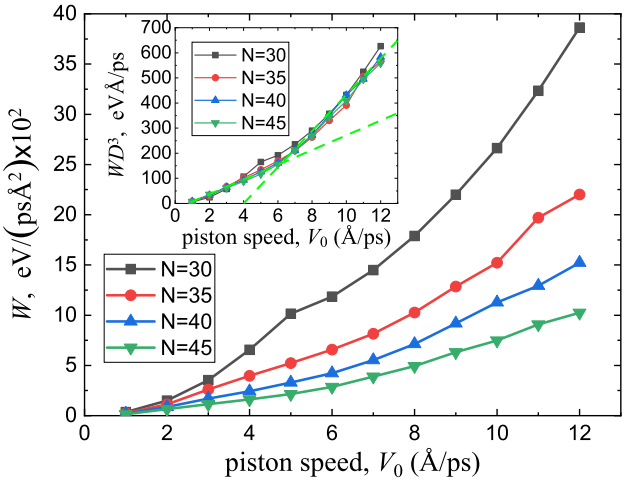

Figure 9. Energy absorption rate as a function of piston speed V_0 for bundles with CNTs of different diameters, which is controlled by the number of carbon atoms in the cross section N. The inset shows the rate of energy absorption multiplied by the cube of the CNT diameter. The green dashed lines show the bilinear fit.

that effectively convert the impact energy into the energy of thermal vibrations. Overall, the results of this study can be useful in the design of elastic dampers.

In the present study only single-walled CNTs of the same diameter were considered. Since the CNTs are often double- and triple-walled, and there is always a dispersion of diameters in the bundle, the study of the absorption of shock wave energy in such systems seems to be a natural continuation of this work. The entanglement of CNTs cannot be taken into account within the framework of the chain model used here, and full atomic MD modeling or another approach must be implemented.

ACKNOWLEDGEMENTS

For A.M.B. and S.V.D. this work was carried out with financial support from the Russian Science Foundation, grant no. 21-19-00813. E.A.K. is grateful for the financial support to the Grants Council of the President of the Russian Federation grant NSh-4320.2022.1.2.

[1] Treacy, M.M.J.; Ebbesen, T.W.; Gibson, J.M. Exceptionally high Young's modulus observed for individual carbon nanotubes, *Nature* **1996** *381*, 678–680.

[2] Wong, E.W.; Sheehan, P.E.; Lieber, C.M. Nanobeam mechanics: Elasticity, strength, and toughness of nanorods and nanotubes. *Science* **1997** *277*, 1971–1975.

[3] Hecht, D.S.; Hu, L.; Irvin, G. Emerging transparent electrodes based on thin films of carbon nanotubes, graphene, and metallic nanostructures. *Advanced Materials* **2011** *23*, 1482–1513.

[4] Popov, V.N. Carbon nanotubes: Properties and application. *Materials Science and Engineering R: Reports* **2004** *43*, 61–102.

[5] Katin,K.P. ; Maslov, M.M.; Krylov, K.S.; Mur, V.D. On the impact of substrate uniform mechanical tension on the graphene electronic structure. *Materials* **2020** *13*, 4683.

[6] Li, M.; Mu, B. Effect of different dimensional carbon materials on the properties and application of phase change materials: A review. *Applied Energy* **2019** *242*, 695–715.

[7] Biercuk, M.J.; Llaguno, M.C.; Radosavljevic, M.; Hyun, J.K.; Johnson, A.T.; Fischer, J.E. Carbon nanotube composites for thermal management. *Applied Physics Letters* **2002** *80*, 2767–2769.

[8] Li, Y.; Huang, X.; Zeng, L.; Li, R.; Tian, H.; Fu, X.; Wang, Y.; Zhong, W.-H. A review of the electrical and mechanical properties of carbon nanofiller-reinforced polymer composites. *Journal of Materials Science* **2019** *54*, 1036–1076.

[9] Chawla, R.; Sharma, S. Molecular dynamics simulation of carbon nanotube pull-out from polyethylene matrix. *Composites Science and Technology* **2017** *144*, 169–177.

[10] Chen, X.; Paul, R.; Dai, L. Carbon-based supercapacitors for efficient energy storage. *National Science Review* **2017** *4*, 453–489.

[11] Afzal, A.; Abuilaiwi, F.A.; Habib, A.; Awais, M.; Waje, S.B.; Atieh, M.A. Polypyrrole/carbon nanotube supercapacitors. Technological advances and challenges. *Journal of Power Sources* **2017** *352*, 174–186.

[12] Wang, B.; Huang, W.; Chi, L.; Al-Hashimi, M.; Marks, T.J.; Facchetti, A. High- k gate dielectrics for emerging flexible and stretchable electronics. *Chemical Reviews* **2018** *118*, 5690–5754.

[13] Tornabene, F.; Fantuzzi, N.; Bacciocchi, M. Linear static response of nanocomposite plates and shells reinforced by agglomerated carbon nanotubes. *Composites Part B: Engineering* **2017** *115*, 449–476.

[14] Prudkovskiy, V.S.; Iacovella, F.; Katin, K.P.; Maslov, M.M.; Cherkashin, N. A bottom-up approach for controlled deformation of carbon nanotubes through blistering of supporting substrate surface. *Nanotechnology* **2018**, *29*, 365304.

[15] Yu, M.-F.; Files, B.S.; Arepalli, S.; Ruoff, R.S. Tensile loading of ropes of single wall carbon nanotubes and their mechanical properties. *Phys. Rev. Lett.* **2000**, *84*, 5552–5555.

[16] Islam, S.; Saleh, T.; Asyraf, M.R.M.; Mohamed Ali, M.S. An ex-situ method to convert vertically aligned carbon nanotubes array to horizontally aligned carbon nanotubes mat. *Mater. Res. Express* **2019**, *6*, 025019.

[17] Zhang, R.; Zhang, Y.; Wei, F. Horizontally aligned carbon nanotube arrays: Growth mechanism, controlled synthesis, characterization, properties and applications. *Chem. Soc. Rev.* **2017**, *46*, 3661–3715.

[18] Nam, T.H.; Goto, K.; Yamaguchi, Y.; Premalal, E.V.A.; Shimamura, Y.; Inoue, Y.; Naito, K.; Ogihara, S. Effects of CNT diameter on mechanical properties of aligned CNT sheets and composites. *Compos. Part A Appl. Sci. Manuf.* **2015**, *76*, 289–298.

[19] Qiu, L.; Wang, X.; Su, G.; Tang, D.; Zheng, X.; Zhu, J.; Wang, Z.; Norris, P.M.; Bradford, P.D.; Zhu, Y. Remarkably enhanced thermal transport based on a flexible horizontally-aligned carbon nanotube array film. *Sci. Rep.* **2016**, *6*, 21014.

[20] Drozdov, G.; Ostanin, I.; Xu, H.; Wang, Y.; Dumitrică, T.; Grebenko, A.; Tsapenko, A.P.; Gladush, Y.; Ermolaev, G.; Volkov, V.S.; Eibl, S.; Rüde, U.; Nasibulin, A.G. Densification of single-walled carbon nanotube films: Mesoscopic distinct element method simulations and experimental validation. *J. Appl. Phys.* **2020**, *128*, 184701.

[21] Xu, H.; Drozdov, G.; Park, J.G.; Jensen, B.D.; Wise, K.E.; Liang, Z.; Odegard, G.M.; Siochi, E.J.; Dumitrică, T. Computationally guided design of large-diameter carbon nanotube bundles for high-strength materials. *ACS Appl. Nano Mater.* **2021**, *4*, 11115–11125.

[22] Grebenko, A.K.; Drozdov, G.; Gladush, Y.G.; Ostanin, I.; Zhukov, S.S.; Melentyev, A.V.; Khabushev, E.M.; Tsapenko, A.P.; Krasnikov, D.V.; Afinogenov, B.; Temiryazev, A.G.; Dremov, V.V.; Dumitricã, T.; Li, M.; Hijazi, H.; Podzorov, V.; Feldman, L.C.; Nasibulin, A.G. Local ultra-densification of single-walled carbon nanotube films: Experiment and mesoscopic modeling. *Carbon* **2022**, *196*, 979–987.

[23] Tang, J.; Sasaki, T.; Yudasaka, M.; Matsushita, A.; Iijima, S. Compressibility and polygonization of single-walled carbon nanotubes under hydrostatic pressure. *Phys. Rev. Lett.* **2000**, *85*, 1887–1889.

[24] Karmakar, S.; Sharma, S.M.; Teredesai, P.V.; Muthu, D.V.S.; Govindaraj, A.; Sikka, S.K.; Sood, A.K. Structural changes in single-walled carbon nanotubes under non-hydrostatic pressures: X-ray and Raman studies. *New J. Phys.* **2003**, *5*, 143.1–143.11.

[25] Qian, D.; Wagner, G.J.; Liu, W.K.; Yu, M.-F.; Ruoff, R.S. Mechanics of carbon nanotubes. *Appl. Mech. Rev.* **2002**, *55*, 495–532.

[26] Silva-Santos, S.D.; Alencar, R.S.; Aguiar, A.L.; Kim, Y.A.; Muramatsu, H.; Endo, M.; Blanchard, N.P.; San-Miguel, A.; Souza Filho, A.G. From high pressure radial collapse to graphene ribbon formation in triple-wall carbon nanotubes. *Carbon* **2019**, *141*, 568–579.

[27] Tangney, P.; Capaz, R.B.; Spataru, C.D.; Cohen, M.L.; Louie, S.G. Structural transformations of carbon nanotubes under hydrostatic pressure. *Nano Lett.* **2005** *5*, 2268–2273.

[28] Zhang, S.; Khare, R.; Belytschko, T.; Hsia, K.J.; Mielke, S.L.; Schatz, G.C. Transition states and minimum energy pathways for the collapse of carbon nanotubes. *Phys. Rev. B* **2006**, *73*, 075423.

[29] Shima, H.; Sato, M. Multiple radial corrugations in multiwalled carbon nanotubes under pressure. *Nanotechnology* **2008**, *19*, 495705.

[30] Zhao, Z.S.; Zhou, X.-F.; Hu, M.; Yu, D.L.; He, J.L.; Wang, H.-T.; Tian, Y.J.; Xu, B. High-pressure behaviors of carbon nanotubes. *J. Superhard Mater.* **2012**, *34*, 371–385.

[31] Baimova, J.A.; Dmitriev, S.V.; Zhou, K. Strain-induced ripples in graphene nanoribbons with clamped edges. *Phys. Status Solidi B* **2012** *249*, 1393–1398.

[32] Lee, J.H.; Loya, P.E.; Lou, J.; Thomas, E.L. Dynamic mechanical behavior of multilayer graphene via supersonic projectile penetration. *Science* **2014** *346*, 1092–1096.

[33] Yoon, K.; Ostadhossein, A.; Van Duin, A.C.T. Atomistic-scale simulations of the chemomechanical behavior of graphene under nanoprojectile impact. *Carbon* **2016** *99*, 58–64.

[34] Haque, B.Z.; Chowdhury, S.C.; Gillespie, J.W. Molecular simulations of stress wave propagation and perforation of graphene sheets under transverse impact. *Carbon* **2016** *102*, 126–140.

[35] Hosseini-Hashemi, S.; Sepahi-Boroujeni, A.; Sepahi-Boroujeni, S. Analytical and molecular dynamics studies on the impact loading of single-layered graphene sheet by fullerene. *Appl. Surf. Sci.* **2018** *437*, 366–374.

[36] Yang, L.; Tong, L. Suspended monolayer graphene traps high-speed single-walled carbon nanotube. *Carbon* **2016** *107*, 689–695.

[37] Shepelev, I.A.; Chetverikov, A.P.; Dmitriev, S.V.; Korznikova, E.A. Shock waves in graphene and boron nitride. *Comp. Mater. Sci.* **2020** *177*, 109549.

[38] Noël, M.; Ananev, S.; Mases, M.; Devaux, X.; Lee, J.; Evdokimov, I.; Dossot, M.; Mcrae, E.; Soldatov, A.V. Probing structural integrity of single walled carbon nanotubes by dynamic and static compression. *Physica Status Solidi - Rapid Research Letters* **2014** *8*, 935–938.

[39] Lahiri, D.; Das, S.; Choi, W.; Agarwal, A. Unfolding the damping behavior of multilayer graphene membrane in the low-frequency regime. *ACS Nano* **2012** *6*, 3992–4000.

[40] Liu, X.; Wang, F.; Wu, H.; Wang, W. Strengthening metal nanolaminates under shock compression through dual effect of strong and weak graphene interface. *Applied Physics Letters* **2014** *104*, 231901.

[41] Woellner, C.F.; Machado, L.D.; Autreto, P.A.S.; De Sousa, J.M.; Galvao, D.S. Structural transformations of carbon and boron nitride nanoscrolls at high impact collisions. *Physical Chemistry Chemical Physics* **2018** *20*, 4911–4916.

[42] Bizao, R.A.; Machado, L.D.; De Sousa, J.M.; Pugno, N.M.; Galvao, D.S. Scale effects on the ballistic penetration of graphene sheets. *Scientific Reports* **2018** *8*, 6750.

[43] Randjbaran, E.; Majid, D.L.; Zahari, R.; Sultan, M.T.H.; Mazlan, N. Effects of volume of carbon nanotubes on the angled ballistic impact for carbon kevlar hybrid fabrics. *Facta Universitatis, Series: Mechanical Engineering* **2020** *18*, 229–244.

[44] Park, S.J., Shin, J., Magagnosc, D.J., Kim, S., Cao, C., Turner, K.T., Purohit, P.K., Gianola, D.S., Hart, A.J. Strong, ultralight nanofoams with extreme recovery and dissipation by manipulation of internal adhesive contacts. *ACS Nano* **2020** *14*, 8383–8391. DOI: 10.1021/acsnano.0c02422

[45] El Moumen, A., Tarfaoui, M., Nachtane, M., Lafdi, K. Carbon nanotubes as a player to improve mechanical shock wave absorption. *Composites Part B: Engineering* **2019** *164*, 67–71. DOI: 10.1016/j.compositesb.2018.11.072

[46] Abdullah, M.F., Abdullah, S., Sohaimi, R.M., Faidzi, M.K. Ballistic resistance of magnesium alloy, AZ31B reinforced with carbon nanotube and lead under gas gun simulation. *Defence S and T Technical Bulletin* **2019** *12*, 311–317.

[47] Kim, J.J., Brown, A.D., Bakis, C.E., Smith, E.C. Hybrid carbon nanotube - carbon fiber composites for high damping. *Composites Science and Technology* **2021** *207*, 108712. DOI: 10.1016/j.compscitech.2021.108712

[48] Vinyas, M., Harursampath, D., Kattimani, S.C. On vibration analysis of functionally graded carbon nanotube reinforced magneto-electro-elastic plates with different electro-magnetic conditions using higher order finite element methods. *Defence Technology* **2021** *17*, 287–303. DOI: 10.1016/j.dt.2020.03.012

[49] Liu, X.-S., Fu, Q.-G., Wang, H.-H., Tong, M.-D., Zhang, J.-P., Song, Q. Improving thermal shock and ablation resistance of high thermal conductivity carbon/carbon composites by introducing carbon nanotubes. *Carbon Letters* **2020** *30*, 721–733. DOI: 10.1007/s42823-020-00144-y

[50] Pourasghar, A., Chen, Z. Heat waves interference regarding dual-phase-lag, hyperbolic and Fourier heat conduction in CNT reinforced composites under a thermal shock. *Waves in Random and Complex Media* **2020** (in press). DOI: 10.1080/17455030.2020.1813351

[51] Alibeigloo, A. Coupled thermoelasticity analysis of carbon nanotube reinforced composite rectangular plate subjected to thermal shock. *Composites Part B: Engineering* **2018** *153*, 445–455. DOI: 10.1016/j.compositesb.2018.09.003

[52] Wittmaack, B.K.; Volkov, A.N.; Zhigilei, L.V. Phase transformation as the mechanism of mechanical deformation of vertically aligned carbon nanotube arrays: Insights from mesoscopic modeling. *Carbon* **2019**, *143*, 587–597.

[53] Wittmaack, B.K.; Volkov, A.N.; Zhigilei, L.V. Mesoscopic modeling of the uniaxial compression and recovery of vertically aligned carbon. *Compos. Sci. Technol.* **2018**, *166*, 66–85.

[54] Yakobson, B.I.; Brabec, C.J.; Bernholc, J. Nanomechanics of carbon tubes: Instabilities beyond linear response. *Phys. Rev. Lett.* **1996**, *76*, 2511–2514.

[55] Rafii-Tabar, H.; Ghavanloo, E.; Fazelzadeh, S.A. Nonlocal continuum-based modeling of mechanical characteristics of nanoscopic structures. *Phys. Rep.* **2016**, *638*, 1–97.

[56] Harik, V.M. Ranges of applicability for the continuum beam model in the mechanics of carbon nanotubes and nanorods. *Solid State Commun.* **2001** *120*, 331–335.

[57] Saether, E.; Frankland, S.J.V.; Pipes, R.B. Transverse mechanical properties of single-walled carbon nanotube crystals. Part I: Determination of elastic moduli. *Compos. Sci. Technol.* **2003**, *63*, 1543–1550.

[58] Ji, J.; Zhao, J.; Guo, W. Novel nonlinear coarse-grained potentials of carbon nanotubes. *J. Mech. Phys. Solids* **2019**, *128*, 79–104.

[59] Impellizzeri, A.; Briddon, P.; Ewels, C.P. Stacking- and chirality-dependent collapse of single-walled carbon nanotubes: A large-scale density-functional study. *Phys. Rev. B* **2019**, *100*, 115410.

[60] Chopra, N.G.; Benedict, L.X.; Crespi, V.H.; Cohen, M.L.; Louie, S.G.; Zettl, A. Fully collapsed carbon nanotubes. *Nature* **1995** *377*, 135–138.

[61] Chang, T. Dominoes in carbon nanotubes. *Phys. Rev. Lett.* **2008**, *101*, 175501.

[62] Maslov, M.M.; Grishakov, K.S.; Gimaldinova, M.A.; Katin, K.P. Carbon vs silicon polyprismanes: A comparative study of metallic sp3-hybridized allotropes. *Fuller. Nanotub. Car. N.* **2020** *28*, 97–103.

[63] Onuoha, C.; Drozdov, G.; Liang, Z.; Odegard, G.M.; Siochi, E.J.; Dumitrică, T. Computational investigation of large-diameter carbon nanotubes in bundles for high-strength materials. *ACS Appl. Nano Mater.* **2020**, *3*, 5014–5018.

[64] Drozdov, G.; Xu, H.; Frauenheim, T.; Dumitrică, T. Densely-packed bundles of collapsed carbon nanotubes: Atomistic and mesoscopic distinct element method modeling. *Carbon* **2019**, *152*, 198–205.

[65] Evazzade, I.; Lobzenko, I.P.; Saadatmand, D.; Korznikova, E.A.; Zhou, K.; Liu, B.; Dmitriev, S.V. Graphene nanoribbon as an elastic damper. *Nanotechnology* **2018**, *29*, 215704.

[66] Cao, A.Y.; Dickrell, P.L.; Sawyer, W.G.; Ghasemi-Nejhad, M.N.; Ajayan, P.M. Super-compressible foamlike carbon nanotube films. *Science* **2005**, *310*, 1307–1310.

[67] Rysaeva, L.K.; Korznikova, E.A.; Murzaev, R.T.; Abdullina, D.U.; Kudreyko, A.A.; Baimova, J.A.; Lisovenko, D.S.; Dmitriev, S.V. Elastic damper based on carbon nanotube bundle. *Facta Univ. Ser. Mech. Eng.* **2020**, *18*, 1–12.

[68] Savin, A.V.; Korznikova, E.A.; Dmitriev, S.V. Scroll configurations of carbon nanoribbons. *Phys. Rev. B* **2015**, *92*, 035412.

[69] Korznikova, E.A.; Rysaeva, L.K.; Savin, A.V.; Soboleva, E.G.; Ekomasov, E.G.; Ilgamov, M.A.; Dmitriev, S.V. Chain model for carbon nanotube bundle under plane strain conditions. *Materials* **2019**, *12*, 3951.

[70] Savin, A.V.; Korznikova, E.A.; Dmitriev, S.V. Dynamics of surface graphene ripplocations on a flat graphite substrate. *Phys. Rev. B* **2019**, *99*, 235411.

[71] Abdullina, D.U.; Korznikova, E.A.; Dubinko, V.I.; Laptev, D.V.; Kudreyko, A.A.; Soboleva, E.G.; Dmitriev, S.V.; Zhou, K. Mechanical response of carbon nanotube bundle to lateral compression. *Computation* **2020** *8*, 27.

[72] Rysaeva, L.K.; Bachurin, D.V.; Murzaev, R.T.; Abdullina, D.U.; Korznikova, E.A.; Mulyukov, R.R.; Dmitriev, S.V. Evolution of the carbon nanotube bundle structure under biaxial and shear strains. *Facta Universitatis, Series: Mechanical Engineering* **2020** *18*, 525–536.

[73] Savin, A.V.; Korznikova, E.A.; Dmitriev, S.V. Simulation of folded and scrolled packings of carbon nanoribbons. *Phys. Solid State* **2015**, *57*, 2348–2355.

[74] Savin, A.V.; Korznikova, E.A.; Lobzenko, I.P.; Baimova, Y.A.; Dmitriev, S.V. Symmetric scrolled packings of multilayered carbon nanoribbons. *Phys. Solid State* **2016**, *58*, 1278–1284.

[75] Savin, A.V.; Korznikova, E.A.; Dmitriev, S.V.; Soboleva, E.G. Graphene nanoribbon winding around carbon nanotube. *Comp. Mater. Sci.* **2017**, *135*, 99–108.

[76] Savin, A.V.; Mazo, M.A. 2D chain models of nanoribbon scrolls. *Adv. Struct. Mater.* **2019**, *94*, 241–262.

[77] Korznikova, E.A.; Zhou, K.; Galiakhmetova, L.K.; Soboleva, E.G.; Kudreyko, A.A.; Dmitriev, S.V. Partial auxeticity of laterally compressed carbon nanotube bundles. *Phys. Status Solidi - RRL* **2022**, *16*, 2100189.

[78] Dmitriev, S.V.; Semenov, A.S.; Savin, A.V.; Ilgamov, M.A.; Bachurin, D.V. Rotobreather in a carbon nanotube bundle. *Journal of Micromechanics and Molecular Physics* **2020**, *5*, 2050010.

[79] Dmitriev, S.V.; Ilgamov, M.A. The radial response of a carbon nanotube to dynamic pressure. *Doklady Physics* **2021**, *66*, 336–340.

[80] Zakharchenko, K.V.; Fasolino, A.; Los, J.H.; Katsnelson, M.I. Melting of graphene: From two to one dimension. *J. Phys. Condens. Matt.* **2011**, *23*, 202202.